

RESEARCH ARTICLE

10.1029/2017JB015419

Key Points:

- Q structure estimated from ambient seismic noise recordings shows some correlation with known geology
- Results suggest that there is a nonlinear relationship between Q and compression
- Estimated Q values may explain poor ambient noise interferometry results for signals crossing the North Sea

Supporting Information:

- Supporting Information S1

Correspondence to:

C. Allmark,
c.allmark@sms.ed.ac.uk

Citation:

Allmark, C., Curtis, A., Galetti, E., & de Ridder, S. (2018). Seismic attenuation from ambient noise across the North Sea Ekofisk permanent array. *Journal of Geophysical Research: Solid Earth*, 123. <https://doi.org/10.1029/2017JB015419>

Received 6 JAN 2018

Accepted 15 AUG 2018

Accepted article online 24 AUG 2018

Seismic Attenuation From Ambient Noise Across the North Sea Ekofisk Permanent Array

Claire Allmark¹ , Andrew Curtis¹ , Erica Galetti¹ , and Sjoerd de Ridder¹

¹School of GeoSciences, Grant Institute, The University of Edinburgh, Edinburgh, UK

Abstract Quality factor (Q) or equivalently attenuation $\alpha = \frac{1}{Q}$ describes the amount of energy lost per cycle as a wave travels through a medium. This is important to correct seismic data amplitudes for near-surface effects, to locate subsurface voids or porosity, to aid seismic interpretation, or for characterizing other rock and fluid properties. Seismic attenuation can be variable even when there are no discernible changes in seismic velocity or density (Yıldırım et al., 2017, <https://doi.org/10.1016/j.jappgeo.2016.11.010>) and so provides independent information about subsurface heterogeneity. This study uses ambient noise recordings made on the Ekofisk Life of Field Seismic array to estimate Q structure in the near surface. We employ the method of X. Liu et al. (2015, <https://doi.org/10.1093/gji/ggv357>), which uses linear triplets of receivers to estimate Q —ours is the first known application of the method to estimate the Q structure tomographically. Estimating Q requires an estimate of phase velocity which we obtain using the method of Bloch and Hales (1968, <https://pubs.geoscienceworld.org/ssa/bssa/article-abstract/58/3/1021/116607/>) followed by travelt ime tomography. The Q structure at Ekofisk has features which can be related to local geology, showing that surface ambient noise recordings may provide a new and robust method to image Q . Our results suggest that there is a nonlinear relationship between Q and compression. They also may explain why it has been found that in the period range of 1 to 2 s considered here, ambient noise cross correlations along paths that span the North Sea Basin are unreliable: Such Q values would attenuate almost all ambient seismic energy during such a traverse.

1. Introduction

All waves that travel through the Earth undergo some form of energy reduction in the dominant direction of propagation, whether due to scattering, energy conversion, or geometrical spreading (Sain et al., 2009; Zhang & Ulrych, 2002). Attenuation is defined as the apparent loss of energy per cycle $\Delta E/E$, where ΔE is the energy lost in each cycle and E is the peak strain energy which is stored in the volume (Aki, 1980; Sain et al., 2009). Attenuation can be described by the quality factor Q , which is a dimensionless quantity that is inversely proportional to attenuation α (Aki & Richards, 1980):

$$\frac{1}{Q(\omega)} = -\frac{\Delta E}{2\pi E} = \alpha(\omega) \quad (1)$$

Seismic energy recorded at a limited array of receivers can be lost due to anelastic (or intrinsic) attenuation or due to medium heterogeneities (scattering) (Allen et al., 2007; Fehler et al., 1992; Frankel & Wennerberg, 1987; Quan & Harris, 1997; Sain et al., 2009; Zhang & Ulrych, 2002). Scattering causes transfer of energy to other directions or later arrivals (and hence is not genuinely reducing kinetic energy, even if it appears to do so), while intrinsic attenuation transfers kinetic energy to heat (Allen et al., 2007; Dasios et al., 2001; Fehler et al., 1992; Pride et al., 2004). Attenuation is known from poroelastic rock physics theory to be frequency dependent with high-frequency components being more rapidly attenuated due to the larger number of cycles per second than lower-frequency components (Beckwith et al., 2016; Chapman et al., 2006; Pride et al., 2004; Quan & Harris, 1997). This shifts the centroid of a signal spectrum toward lower frequencies during propagation, a phenomenon which has been observed clearly, for example, as waves propagate vertically in vertical seismic profiling data (Li et al., 2006; Quan & Harris, 1997; Singhroha et al., 2016).

Seismic attenuation has been shown to be variable even when there are no discernible changes in seismic velocity or density (Yıldırım et al., 2017) and so provides independent information about subsurface heterogeneity. Estimating attenuation is therefore useful in a number of settings: for example, in engineering when analyzing ground conditions and strength, Q can give an indication of soil saturation, the effective stress

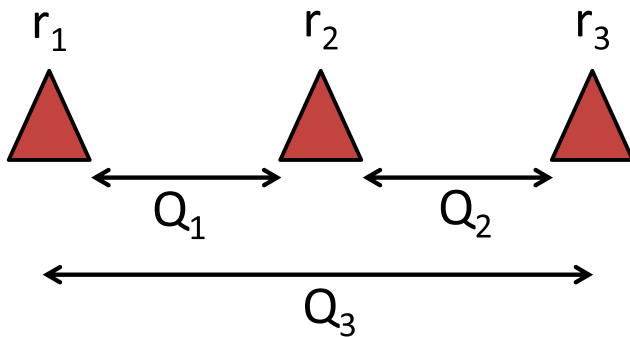


Figure 1. Aligned-triplet receiver geometry and the three Q values which can be estimated from this arrangement, one between each pair of receivers.

state, inherent and stress induced anisotropy, and cementation (Oelze et al., 2001; Priest et al., 2006; Rodríguez-Pradilla, 2015; Xia, 2014). It can also be used to locate subsurface structures such as when investigating the presence of tunnels or mine workings, as tunnels and any subsurface void cause Q anomalies (Morton et al., 2016). Q is also used in Amplitude Versus Offset analysis to compensate for seismic wave attenuation (Dasgupta & Clark, 1998; Sain et al., 2009; Zhang & Ulrych, 2002) and in seismic hazard analysis and earthquake engineering to estimate ground acceleration due to earthquakes, as attenuation must be taken into account when predicting wave amplitudes (Allen et al., 2007; Joshi, 2007; McNamara et al., 2014; Parolai, 2014; Raghu Kanth & Iyengar, 2007). It can be used as an indicator of the presence of hydrocarbons (Carcione, 2000; Dasgupta & Clark, 1998; Dvorkin & Mavko, 2006) or for correcting seismic data to improve resolution when using standard imaging techni-

ques (Zhang & Ulrych, 2002). Q is particularly useful in the characterization of rock and fluid properties and is sensitive to a number of factors, such as disruption in the medium due to faults, fractures, and weathering, which all act to reduce Q (Rodríguez-Pradilla, 2015; Rubino et al., 2014), porosity and pore fluid parameters, temperature, density, pressure, lithology, and others (Gei & Carcione, 2003; Prasad & Manghnani, 1997; Quan & Harris, 1997; Sain et al., 2009; Yildirim et al., 2017). When used in addition to seismic velocity analysis, Q can provide complimentary information on rock properties (Ekanem et al., 2013; E. Liu et al., 2007; Maultzsch et al., 2007; Quan & Harris, 1997), and Prasad and Manghnani (1997) found that Q was more sensitive than compressional wave seismic velocity to effects of pore pressure and pore space deformation.

Many studies have been carried out that aim to produce reliable Q structure estimates using a variety of methods. Most make use of absolute signal amplitudes, but this information is often inaccurate due to noise, geometrical spreading, scattering, and other effects (Zhang & Ulrych, 2002). Sain et al. (2009) estimated Q for marine multichannel seismic data using a method based on the logarithm of the spectral ratio. They applied the method to the western margin of India where it is known that gas hydrates exist, which have been shown to have a strong influence on Q (Rossi et al., 2007; Sain et al., 2009; Singhroha et al., 2016). Zhang and Ulrych (2002) use prestack data to estimate Q using common midpoint gathers and a layer stripping approach, while Yildirim et al. (2017) estimate Q using four different methods: amplitude decay, spectral ratio, Wiener filters, and artificial neural networks. The four methods were first tested with synthetic data and then applied to high-resolution seismic reflection data collected in the Arnavutköy district of Istanbul, Turkey; their results showed that artificial neural network was the most reliable method, while amplitude decay was most sensitive to noise. Beckwith et al. (2016) introduced a method that uses pairs of reflections in prestack τ - p domain surface seismic data to measure frequency-dependent Q . They modeled the frequency dependence as the power law $Q(f) = a f^b$. Their results from synthetic data gave robust estimates of frequency-dependent Q ; however, when they applied the method to data from the North Sea their results indicated that Q had little dependence on frequency.

Methods to estimate attenuation from ambient seismic noise data have also been developed (e.g., Lawrence & Prieto, 2011; Lin et al., 2011; Prieto et al., 2011). In this study we apply the method presented by X. Liu et al. (2015) to estimate Q using linear triplets of receivers. In comparison to the methods described above, this method is designed specifically for ambient seismic noise data, which means that it has been designed for use with randomly directed surface waves. From a linear array of three receivers arranged as shown in Figure 1, the method estimates three Q values, one between each receiver pair. Although the method of X. Liu et al. (2015) accounts for different site amplification factors at the three receivers, these cannot be estimated independently. Therefore, in our application, we make the assumption that site amplification factors are equal across the array. X. Liu et al. (2015) showed when using synthetic data that when there is a nonisotropic source distribution and the maximum noise intensity is oriented along the interstation path, all three Q values can be estimated reliably. However, given an isotropic source distribution, only the Q_3 estimate is reliable, while Q_1 and Q_2 are subject to trade-offs. Since the noise distribution in our application is reasonably isotropic when averaged over time, we use the method to estimate Q_3 only.

We begin by explaining the method of X. Liu et al. (2015) and outline how the prerequisite phase velocity is estimated herein. We then present results from the Ekofisk Life of Field Seismic (LoFS) array at three

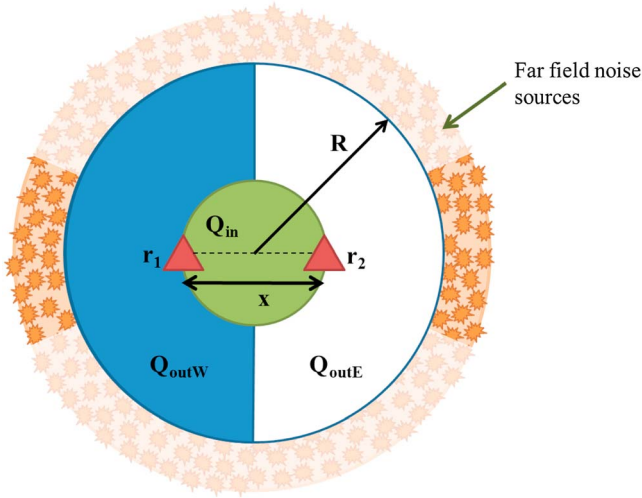


Figure 2. Receivers r_1 and r_2 (triangles) in a solid with attenuation defined by three Q values: Q_{in} between the receivers (green), and Q_{outW} (blue) and Q_{outE} (white) in the bounding regions to the west and east, respectively. It is assumed that there are only far-field noise sources at approximate distance R from the origin, shown by the orange ring. Sources outside of the stationary phase region of the direct wave between the receiver locations contribute less to the cross correlation of recordings made at r_1 and r_2 and so have muted shading. Reproduced from X. Liu et al. (2015).

frequencies and discuss the correlation of these results with known geological features. To conclude, we argue that by using ambient noise recordings made on linear triplets of receivers, we are able to produce a Q structure which is clearly related to known geological features and hence which appears to be reliable.

2. Q Estimation Using Linear Triplets of Receivers

While the method to estimate Q requires a triplet of receivers, the underlying theory is best explained using two receivers at a time. Receivers r_1 and r_2 from Figure 1 are used for this purpose. We assume that the two receivers, separated by distance x , are in a solid defined by three Q values as shown in Figure 2. The area between the two receivers is defined by Q_{in} (green area), and the bounding regions to the west and east are defined by Q_{outW} (blue) and Q_{outE} (white). We assume that there are only far-field noise sources at distance R from the origin shown by the orange ring. We aim to estimate Q_{in} while allowing different Q values to exist to the west and east.

The method is designed for use with ambient noise cross correlations and hence for surface waves—the dominant component of ambient noise as most noise sources are located on the Earth’s surface (Curtis et al., 2006; Gouédard et al., 2008; Halliday & Curtis, 2008; Nicolson et al., 2012; Saygin et al., 2015). At the two receivers we record the wavefields from the boundary of randomly firing, temporally uncorrelated sources, which

we denote as u_1 and u_2 in the frequency domain for receivers r_1 and r_2 , respectively.

The first step is to calculate the cross correlation of the two noise recordings. Due to the stationary phase approximation (Halliday & Curtis, 2009; Snieder, 2004; Snieder et al., 2006), sources in the region aligned with the interreceiver path (Figure 2) have the greatest contribution to the cross correlation, while other sources cancel destructively. The cross correlation in the frequency domain, called the *cross spectrum*, is denoted $C_{u_1u_2}$. Receiver r_1 at position $-\frac{x}{2}$ is treated as a virtual source which is recorded at receiver r_2 at position $\frac{x}{2}$. If we assume that x , the interreceiver distance, is much greater than the wavelength, then the expanded value of the cross spectrum between the two receivers can be described by (X. Liu et al., 2015)

$$E\left\{C_{u_1u_2}\left(-\frac{x}{2}, \frac{x}{2}; \omega\right)\right\} = \pi\beta_1\beta_2B(\omega)\sqrt{\frac{i2c(\omega)}{\pi\omega\chi\varepsilon_W}}\exp\left[-\omega\left(\frac{R-\frac{x}{2}}{c(\omega)Q_{outW}} + \frac{x}{2c(\omega)Q_{in}}\right)\right]\exp\left[-i\frac{\omega x}{c(\omega)}\right] \\ + \pi\beta_1\beta_2B(\omega)\sqrt{-\frac{i2c(\omega)}{\pi\omega\chi\varepsilon_E}}\exp\left[-\omega\left(\frac{R-\frac{x}{2}}{c(\omega)Q_{outE}} + \frac{x}{2c(\omega)Q_{in}}\right)\right]\exp\left[j\frac{\omega x}{c(\omega)}\right] \quad (2)$$

where β_1 and β_2 are the real-valued frequency-dependent site amplification factors, which account for effects on the surface wave amplitude of local velocity and density structure beneath the receiver (Lin et al., 2012), and $B(\omega)$ is the noise source power spectral density which is the cross correlation of the source signatures. The terms with the square root are amplitude correction factors, containing terms ε_W and ε_E , which account for the rotation of the phase angle due to attenuation, and c which is the phase velocity. The first exponential in each term is the attenuation term, and the second exponential is the phase term. The equation is divided into the causal (first term on the right) and acausal (second term on the right) parts. Only noise propagating from the west is relevant for the causal part, which means only Q_{outW} and Q_{in} are relevant; for the acausal part only noise propagating from the east is relevant, that is, only attenuation terms Q_{outE} and Q_{in} .

For the three-receiver aligned triplet geometry in Figure 1 we denote the spectra recorded at the three receivers by u_1 , u_2 , and u_3 , the cross spectrum of u_1 and u_2 by $C_{u_1u_2}$ and equivalently for the other receiver pairs. We measure amplitudes on the causal part of the cross correlation and apply the appropriate amplitude correction from the square root terms in equation (2). This gives us the corrected causal amplitude decay curve for receivers r_1 and r_2 :

$$\widehat{C}_{u_1 u_2}^+(\omega) = \frac{C_{u_1 u_2}^+(\omega)}{\sqrt{\frac{12c(\omega)}{\pi\omega x \varepsilon_W}}} \quad (3)$$

We obtain similar expressions using the other receiver pairs for $\widehat{C}_{u_1 u_3}^+(\omega)$ and $\widehat{C}_{u_2 u_3}^+(\omega)$.

The aim of using equation (2) is to estimate Q_1 , Q_2 , and Q_3 , so this means we must either know or be able to cancel the other variables. Some of the variables are known: ω is the current frequency of analysis, and x is the interreceiver distance. Further parameters can be fixed by making some assumptions. We assume that the attenuation is not great enough to cause significant rotation of the phase angle, an assumption which is true for most practical cases (X. Liu et al., 2015), so we set the values ε_W and ε_E to 1. By taking differences of the natural logarithms of the three spectra, we can further simplify the problem by canceling terms in equation (2) containing B , R , and $Q_{\text{outE/W}}$. This differencing process leaves us with three equations, one for each Q value shown in Figure 1:

$$\begin{aligned} \ln \widehat{C}_{u_2 u_3}^+(\omega) - \ln \widehat{C}_{u_1 u_3}^+(\omega) &= \frac{-\omega x_1}{2c_1(\omega)Q_1} + \frac{\gamma_2}{1} \\ \ln \widehat{C}_{u_1 u_3}^+(\omega) - \ln \widehat{C}_{u_1 u_2}^+(\omega) &= \frac{-\omega x_2}{2c_2(\omega)Q_2} + \frac{\gamma_3}{2} \\ \ln \widehat{C}_{u_2 u_3}^+(\omega) - \ln \widehat{C}_{u_1 u_2}^+(\omega) &= \frac{-\omega x_3}{2c_3(\omega)Q_3} + \frac{\gamma_3}{1} \end{aligned} \quad (4)$$

in which x_1 , x_2 , and x_3 are the distances between receivers r_1 and r_2 , r_2 and r_3 , and r_1 and r_3 , respectively, and similarly for the phase velocities, c_1 , c_2 , and c_3 . These equations all contain the terms γ , which are the natural logarithms of the ratios of the site amplification factors, for example,

$$\gamma_2 = \ln \left(\frac{\beta_2}{\beta_1} \right) \quad (5)$$

We make a second assumption that over the area of the array the site amplification factors are approximately equal. This means that when we use differences of the three spectra, the ratios of β terms cancel; that is, the γ values in equation (4) are 0 because they are the natural logarithm of 1. This assumption may not be true in practice, but as we only have sufficient constraints to either estimate Q or γ , we choose to fix γ and so assume smooth site amplification. We return to the trade-off relations between Q and γ in section 7. This leaves us with the phase velocities, c_1 , c_2 , and c_3 which can be estimated using a number of published methods, and Q_1 , Q_2 , and Q_3 which we ultimately wish to estimate.

In order to avoid the effects of random fluctuations in amplitude spectra, we find an average Q value for a narrow frequency band; that is, the values of ω span a narrow band of frequencies rather than estimating Q using the amplitude value of a single frequency. By using a finite band, any effects of noise at a single frequency may be averaged out. We estimate Q_3 for every receiver triplet from our receiver array which fall on a straight line, then use ray paths traced during the phase velocity estimation step (see below) to estimate Q maps by performing a linearized least squares tomographic inversion. For all the receiver triplet combinations available, the angle created by the three receivers in Figure 1 was calculated. If the angle between the three receivers was greater than 170° , then the triplet was used in the processing. This minimum angle proved sufficiently large to approximate a straight line for the distances considered here.

3. Phase Velocity Estimation

In order to estimate Q from equation (4), we first need to estimate the phase velocity structure. To this end we estimate average phase velocities between each pair of receivers using the cross-correlation method of Bloch and Hales (1968). This method requires a source in line with two receivers, which is the same geometry as we require to estimate Q if we treat one of the end receivers as a virtual source. In this explanation we will treat receiver r_1 as the virtual source and estimate the phase velocity between receivers r_2 and r_3 .

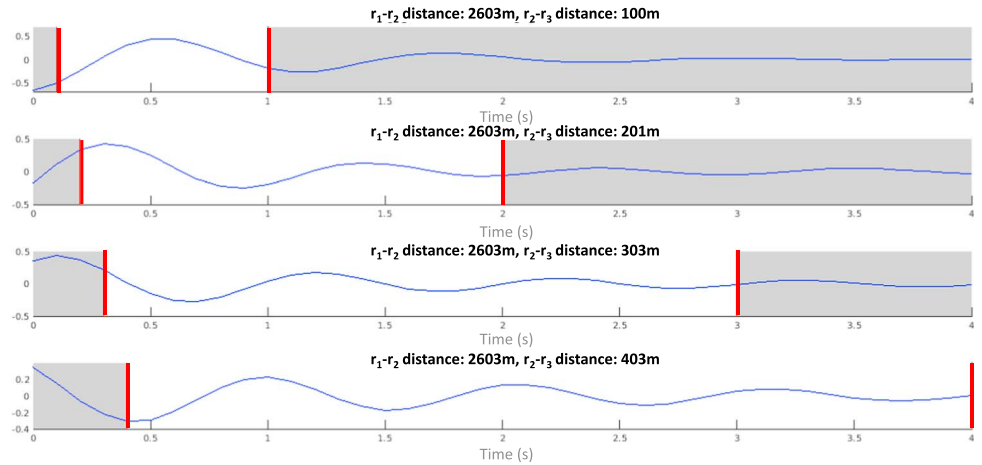


Figure 3. Examples of cross correlations of the windowed filtered seismograms at 0.6 Hz used to estimate phase velocity between receiver pairs r_2 and r_3 , where these are separated by 100, 201, 303, and 403 m for the traces ordered from top to bottom. The red lines mark the time windows in which peaks can be chosen when we define an allowed velocity range of 100 to 1,000 m/s. Peaks are therefore chosen only in areas that are not shaded in gray.

The first step is to measure the group travel time for the two virtual seismograms S_2 between receivers r_1 and r_2 , and S_3 between receivers r_1 and r_3 . Group velocity v_g is defined as the velocity with which each narrow-bandwidth wave energy packet travels, while phase velocity v_{ph} is the velocity with which each single-frequency phase front travels through the medium. These velocities are related by

$$v_g = v_{ph} \left(1 - k \frac{\partial v_{ph}}{\partial \omega} \right)^{-1} \quad (6)$$

(Shearer, 2009). We estimate the group travel time using the multiple filter technique (Bhattacharya, 1983; Dziewonski et al., 1969), a method which estimates the time at which most energy arrives for each frequency band isolated by narrow band-pass filtering seismograms around each current frequency of analysis. After estimating the group travel time for each virtual seismogram S_2 and S_3 , we window the virtual seismograms in time around their group arrival travel times, then reapply a narrow band-pass filter centered on the particular frequency of analysis. We then cross correlate the two windowed filtered seismograms. Since cross correlation involves differencing the phase angles of the two seismograms, one of the peaks of this cross correlation indicates the phase difference which corresponds to the phase travel time between r_1 and r_2 . Since we can estimate the ray path length between the two receivers, we can then infer the corresponding phase velocity between receivers r_1 and r_2 (Bloch & Hales, 1968).

Figure 3 shows four examples of cross correlations of the windowed filtered seismograms for different interreceiver distances. We need to choose the time of a peak in the cross correlation that corresponds to the phase travel time. However, as shown in Figure 3 there are many peaks on the cross correlations and there is no indication of which to choose.

To allow the correct peak to be identified, we use two closely spaced receivers at r_2 and r_3 and define an allowed seismic velocity range as a priori knowledge. In this example we chose a velocity range between 100 and 1,000 m/s; these velocities correspond to the times marked by the red lines on the cross correlation plots in Figure 3 when we assume straight rays between the receivers. The white sections of the cross-correlation plots are the time sections from which we may choose the peaks. At receiver separation between r_2 and r_3 of 100 m (top trace in Figure 3), there is only one peak within the allowed time range, and so we are able to estimate the velocity by choosing this single peak. As the receiver distance increases the number of peaks within the allowed time range increases; at receiver separations of 201 and 303 m there are two peaks within the allowed time range and the number of peaks increases with receiver separation, hence the requirement for closely spaced receivers to estimate phase travel times uniquely.

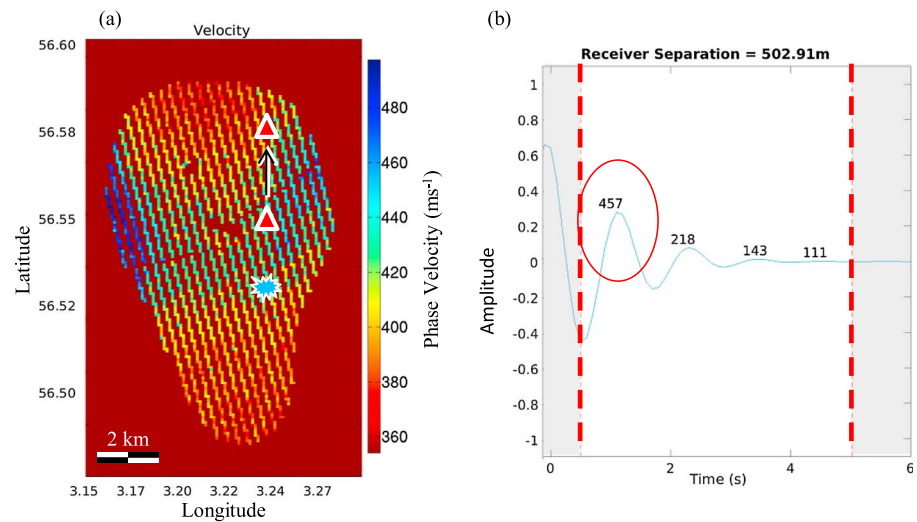


Figure 4. (a) Approximate phase velocity map estimated using all receiver triplets with two closely spaced receivers. Due to the receiver geometry, we only obtained phase velocity estimates for cells lying along the seismic cables. (b) The cross correlation of the windowed filtered seismograms when using receivers separated by 503 m, as shown in (a) where the blue explosion is the virtual source and the triangles are receivers r_1 and r_2 . Peaks are chosen within the white area (bound by the red dashed lines), and average velocities for each peak are estimated based on a straight ray path between the two receivers. These velocities are printed above each peak in meters per second. The approximate map is used to choose the appropriate peak: The average velocity between receivers r_1 and r_2 is 453 m/s; the peak at 457 m/s is therefore closest to this estimate, and so this peak is chosen as the correct phase travel time.

By using all available triplets with two closely spaced receivers and assuming straight ray paths between the receivers, we create an approximate map of phase velocity estimates. Figure 4a shows an example for the Ekofisk LoFS array at 1 Hz. We then use this map to identify the correct peak in the cross correlations when we have receivers with greater separation and hence with multiple peaks to choose from. For example, if we have a virtual source and two receivers with a larger separation, such as those in Figure 4a in which the receivers are separated by 503 m, there are many peaks to choose from. In order to decide which peak should be used, we first find an average velocity between the receivers from the approximate map, by tracing a straight path between the receivers and calculating the average velocity of all the cells traversed for which we have a phase velocity estimate. So if the straight ray path between receivers r_2 and r_3 crosses 10 cells and 5 of those contain a phase velocity estimate from using the receivers with smaller interreceiver spacing, then the velocities estimated in those 5 cells are averaged to produce the initial phase velocity estimate. In the example of Figure 4, the average velocity between the receivers is 453 m/s. The interreceiver cross correlation shown in Figure 4b has many peaks, with their associated phase velocity estimates based on straight rays shown as numbers by each peak. The peak at 457 m/s is closest to 453 m/s, so this peak is chosen as the phase travel time for this receiver pair. This process makes the assumption of straight ray paths throughout as ray geometry estimation requires the velocity structure. This in turn means that the distance used to convert between velocity and travel time is the straight line distance between the two receivers. With the distances considered here the difference between the velocity estimated using straight rays and actual rays should not be large enough to cause the incorrect peak to be chosen. This process is repeated for all receiver triplets within the array which form a straight line.

These phase travel times are then input to the tomography code Fast Marching Surface Tomography (Rawlinson, 2005). This is an iterative linearized tomography method which uses the eikonal equation and the fast marching method for the forward prediction step and a subspace inversion scheme for the inversion step. The code outputs phase velocity maps and corresponding traced ray paths, and from these we can calculate an average phase velocity along the ray path for all receiver pairs that we wish to use. These phase velocities can then be used in equation (4) in order to allow us to estimate the Q values between each receiver pair.

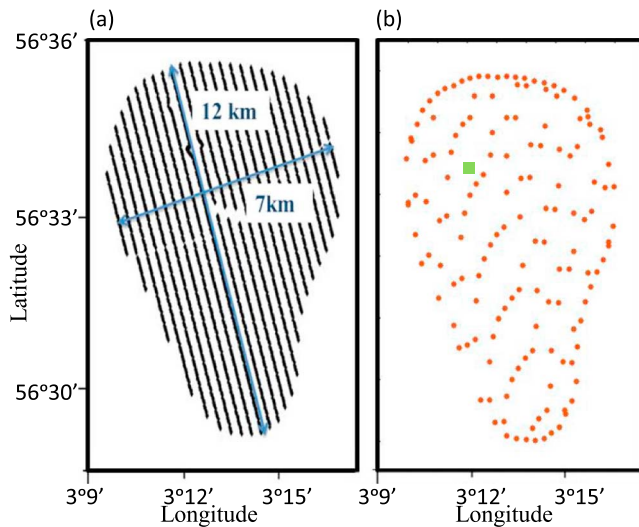


Figure 5. (a) The Ekofisk receiver array; each black dot represents a single receiver. Approximate dimensions of the Ekofisk array are also shown. (b) Geometry of receiver subset chosen for Q value estimation. Each red dot represents a receiver chosen for the Q estimation. Receivers around the array edge were chosen together with every fortieth receiver inside the array. The green square shows the location at which depth inversion was carried out prior to estimating linearized depth sensitivity kernels.

4. Q at the Ekofisk LoFS Array

4.1. The Ekofisk Field

The Ekofisk field is located in the southern part of the Norwegian North Sea, approximately 270 km off the coast of Norway. The field was discovered in 1969, and hydrocarbon production began in 1971 (Bertrand et al., 2014; Zoback & Zinke, 2002). Since production began there has been significant compaction at the field due to the depletion of fluid pressure. This led to seabed subsidence large enough to require substantial elevation of the platforms in 1987 at considerable cost (Bertrand et al., 2014; Zoback & Zinke, 2002).

The field itself is a large four-way dip anticline in the southern Norwegian Central Graben (Gennaro et al., 2013; Zoback & Zinke, 2002). The reservoir itself consists of overpressured and naturally fractured chalk sediments located between 2,900 and 3,250 m with an oil column of greater than 300 m (Gennaro et al., 2013; Nagel, 2001; Zoback & Zinke, 2002). The Maastrichtian Tor and Danian Ekofisk Formations, which consist of resedimented and highly porous chalks, make up the reservoir, and the source rock is the Upper Jurassic Farsund Formation (Gennaro et al., 2013; Zoback & Zinke, 2002). Due to the low permeability of chalk matrices (0.110 mD), production at the Ekofisk field has been enhanced through the use of a network of fractures which have permeability up to 50 mD (Gennaro et al., 2013). At the crest of the field is a seismically obscured area caused by gas which has moved into shallower stratigraphic layers (Gennaro et al., 2013).

A LoFS array was installed at the Ekofisk field in 2010, with 200 km of trenched fiber-optic seismic cables and 3,966 4C sensor stations (Buizard et al., 2013). These cables cover about 60 km² and have intercable spacing of 300 m and a receiver station interval of 50 m. Recordings of ambient seismic noise have been made on these receivers, and this ambient noise data set has been used herein. As we are using data from an ocean bottom array we apply the described method to Scholte waves, which is of what we assume the noise at the area of study consists. This was confirmed by slowness analysis in de Ridder et al. (2015).

In order to cross correlate the ambient noise recordings, the following processing was applied: the recorded pressure data were first band-pass filtered with a flat response in the range 0.4–1.3 Hz and a Hann taper extending 0.5 Hz on either side. Filtering was performed on data segments of 3 min, plus 20 s of overlap between segments, after which the data were restitched together by averaging in the overlap portion. Segments containing noise bursts and spikes were discarded by tapering and substituting zeros in time. All available data were then cross correlated in 10 blocks of 4 hr each, after which the set of cross-correlated blocks were stacked. Processing of ambient seismic noise to produce cross correlations has been discussed in detail in Bensen et al. (2007), and it was this method which we applied to obtain our cross correlations. An example workflow is given in the supporting information.

4.2. Receiver Geometry

We applied the method described above to the Ekofisk LoFS array at three frequencies, 0.5, 0.75, and 1 Hz. The receiver array of 3,966 receivers are arranged as shown in Figure 5a, and a subset of the receivers was chosen to be used to estimate Q as using all combinations of all of the receivers was not practical in terms of computer memory and time; the subset is shown in Figure 5b: We chose receivers around the edge of the array to create a discretized boundary of receivers and inside the array chose every fortieth receiver. This receiver geometry provided good ray path density, as shown in Figure 6. When choosing receiver triplets, the spacing between receivers r_1 and r_2 cannot be significantly greater than the spacing between receivers r_2 and r_3 , and vice versa, as the end fire lobe aperture angle increases with increased interstation distance in the stationary phase approximation (X. Liu et al., 2015). We therefore allow the larger distance to be up to 3 times the smaller of the two distances. This resulted in over 43,000 Q_3 values for each frequency (we assume an isotropic noise distribution and so only used the Q_3 values).

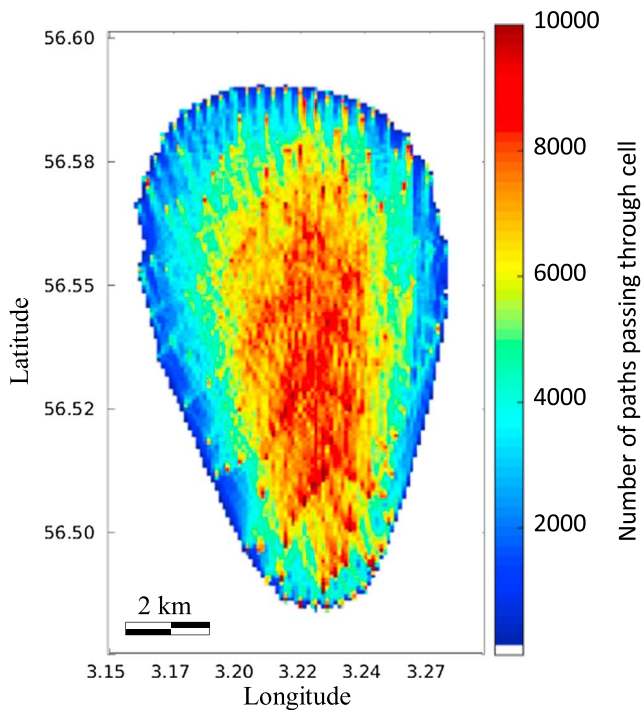


Figure 6. Ray path density at 0.75 Hz using only receiver triplets for which a Q_3 value was estimated. The plotted ray paths show that there is good spatial and azimuthal coverage.

4.3. Phase Velocity Results

Figure 7a shows the phase velocity results at 0.5, 0.75, and 1 Hz. The velocities at 0.5 and 0.75 Hz are higher than those at 1 Hz which is expected as signals at higher frequencies tend to sample shallower parts of the subsurface than lower frequencies. Nevertheless, the structures at all three frequencies are similar: There are low velocities in the south of the array, and there is an area of lower velocity in the center of the array as highlighted in the figure. These common features show continuity of the structure with frequency and therefore presumably with depth. We note that there is greater similarity between the phase velocities at 0.5 and 0.75 Hz than between 0.75 and 1 Hz.

As we use the group velocity in the estimation of the phase velocity, we compare the phase velocity results shown in Figure 7a with the group velocity results shown in Figure 7b. We do not expect the phase and group velocity maps to be the same, due to equation (6); however, there are some common features on the maps. Similarly to the phase velocity, the group velocity shows lower velocities in the center and south of the array at 0.75 and 1 Hz. The phase and group velocity results at 0.75 Hz are most comparable. At 0.5 Hz there are higher group velocities at locations where there are low phase velocities in the center of the array. Similarly to the phase velocities, there are higher group velocities at lower frequencies, again due to the depth range to which the different frequencies are most sensitive.

4.4. Q Results at the Ekofisk Field

The phase velocity maps were used in the estimation of the Q structure, and in our case estimates of phase travel times are made for narrower frequency bands than were the Q estimates. The latter were made for frequency ranges of width 0.1 Hz in order to avoid erroneous effects of random fluctuations in the amplitude spectra. In Figure 7 the phase velocity maps have therefore been plotted for the frequency at the center of the range used for the Q map.

Figure 8 shows the Q results for the three frequency ranges analyzed, which will be identified by their central frequencies, 0.5, 0.75, and 1 Hz. The Q values at 0.5 Hz are much lower than the values at 0.75 and 1 Hz, which are similar in magnitude. That is, the frequency which tends to sample deepest in the subsurface has the lowest Q values. Identifiable features in the results also appear to be quite different for the three frequencies analyzed, but there are some points of common structure which have been highlighted on the maps: maps at 0.5 and 1 Hz show a linear structure of high Q in the north of the array (which also appears faintly at 0.75 Hz), in the center of the array is an undulating ring of high Q surrounding an area of low Q , and there are two zones of low Q at the edges of the array. All three maps also show higher Q values in the south of the array. Thus, again, we see that there are some similarities across different frequencies and therefore presumably across depth ranges.

4.5. Correlation Between Phase Velocity and Q

The phase velocities in Figure 7a were used in the estimation of the Q maps, and a concern might be that these velocities would dominate the Q estimation such that the extra information offered by equation (4) is minimal. However, there appears to be little correlation between the phase velocity and Q structures as shown in Figure 9 which cross-plots Q against phase velocity in each cell. The plot shows that there is no correlation between the results, and hence it does not appear that the phase velocity estimates dominate Q estimates. The amplitude of the cross correlations is affected by the receiver separation, the frequency, Q , and the phase velocity (and any variations in the site amplification factor ratio, although in this case we assume that this is 0). Q and phase velocity are intrinsically linked through the Kramers-Kronig equation (Waters et al., 2005), and it is therefore indeed counterintuitive for the phase velocity and Q not to be correlated. However, the Kramers-Kronig equation does not constrain phase uniquely given the amplitude, and so this explains why the phase velocity and Q maps must not necessarily show similar patterns.

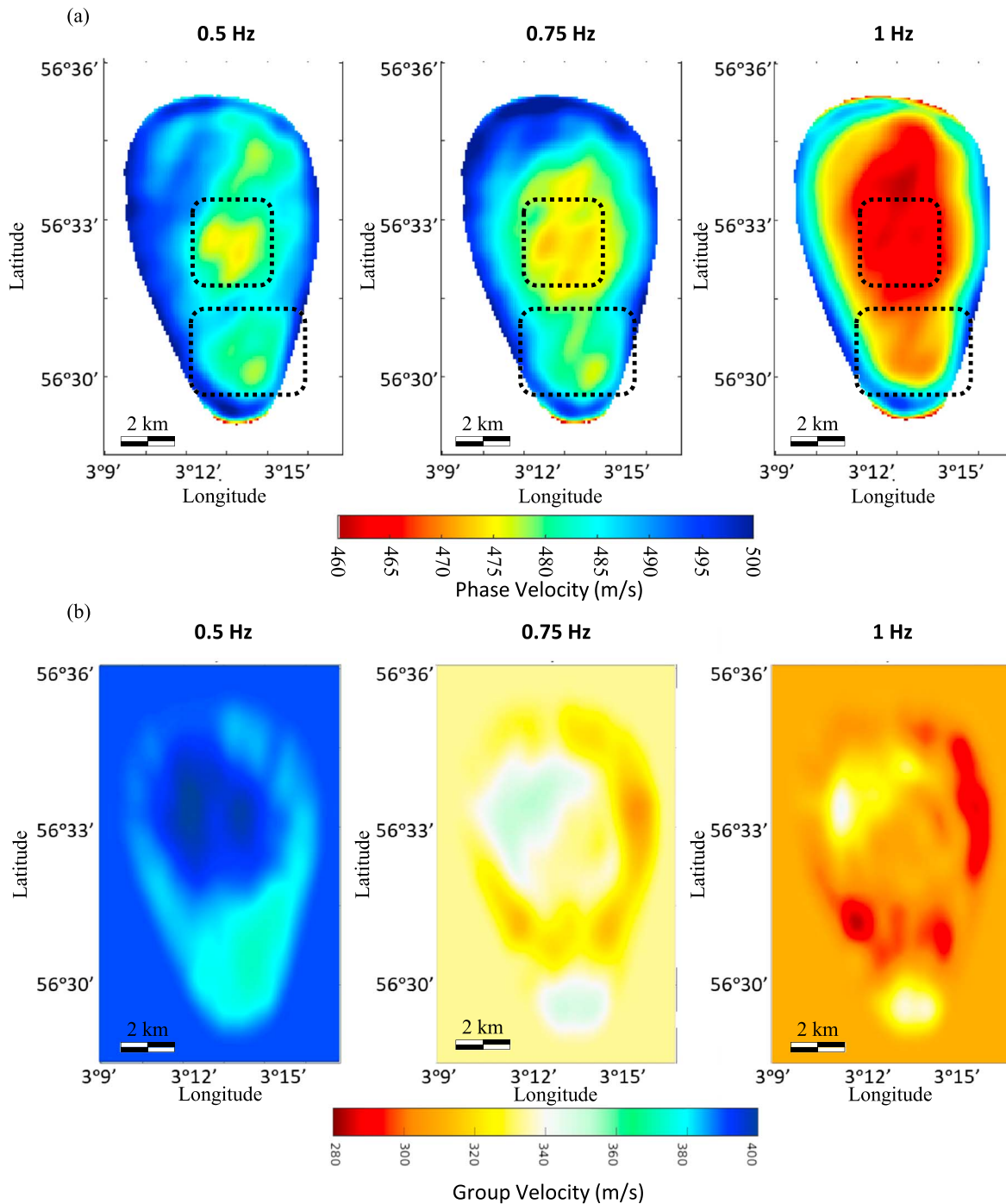


Figure 7. (a) Phase velocity results at 0.5, 0.75, and 1 Hz (left to right) for the Ekofisk array with the receiver geometry shown in Figure 5b. Some common features in the results have been highlighted by dotted rectangles. (b) Corresponding group velocity results at 0.5, 0.75, and 1 Hz for the Ekofisk array with the receiver geometry shown in Figure 5b.

5. Geological Interpretation

In order to validate the Q results, we compare the features observed on the Q maps with known geological features at Ekofisk. In the north of the array is a linear feature of high Q which is highlighted in Figure 8. This linear feature occurs at or close to the location of a known fault marked by a black line in Figure 10. To the north of the fault is an area of high Q , while to the south of the fault is lower Q , apart from in the west of

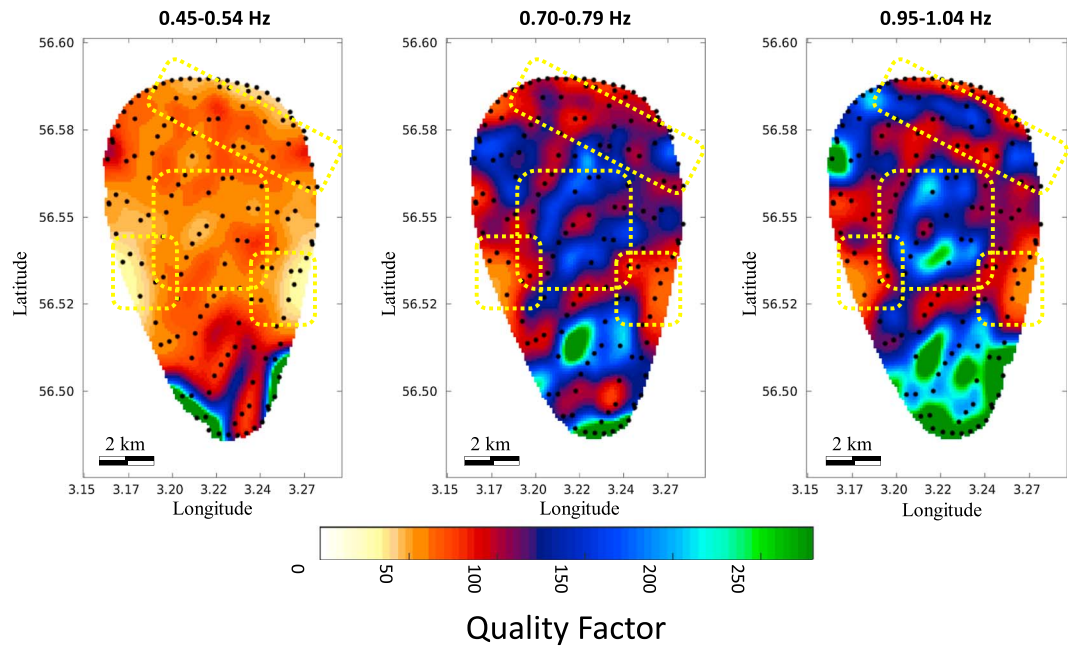


Figure 8. Q results in the frequency ranges 0.45–0.54, 0.70–0.79, and 0.95–1.04 Hz, whose central frequencies correspond to the frequencies for which the phase velocity maps in Figure 7 are shown. Q values at 0.45–0.54 Hz are lower than the Q values at the higher frequencies; however, all three maps show some similar features, which have been highlighted. The black dots show the locations of the receivers used.

the array where this pattern is reversed. At 0.5 Hz the fault separates higher and lower Q similarly to the pattern observed at 1 Hz. However, at 0.75 Hz no such pattern is observed other than in a small area in the east. The observed linear feature is identified with high Q on one side of the fault and low Q on the other side of the fault, thus showing the different structures on either side of the fault.

It is known that there has been subsidence at the Ekofisk field. Ottemöller (2005) presents the subsidence between 1999 and 2001 in their Figure 10, showing that the majority of the subsidence occurred within the reservoir boundary—the white line in Figure 10. Subsidence will likely cause fracturing of the rock, which may cause a reduction in Q . Surprisingly, the Q values seem to show little relation to the large-scale subsidence (even though the group and phase velocities and also their anisotropy are clearly related to subsidence (see Figure 7 and also Barkved et al., 2005; de Ridder et al., 2015; de Ridder & Curtis, 2017). There is a suggestion of a relation in the north of the 1 Hz plot, but nowhere else. However, although clearest on the 1 Hz plot, all results do show a ring of high Q in the center of the array (highlighted in Figure 8) enclosing an area of lower Q .

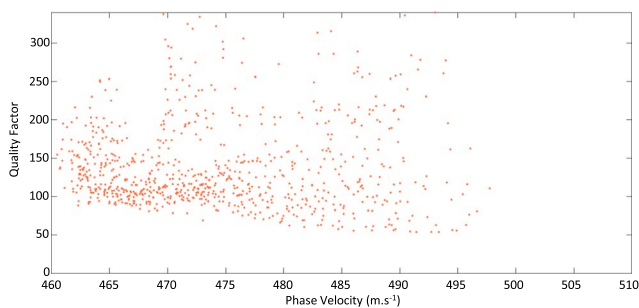


Figure 9. Cross plot of Q against phase velocity for each cell in the model centered at 1 Hz, showing that there is no obvious correlation between the two values.

The ring of high Q is centered around the approximate platform location, which is also known to be the center of subsidence (this is readily observable in Figure 7 of Nagel, 2001). We therefore looked at the correlation of sea floor mean curvature (H) (Goldman, 2005) with Q . Curvature is estimated using

$$2H = \frac{\left(1 + \left(\frac{\partial S}{\partial x}\right)^2\right) \frac{\partial^2 S}{\partial y^2} - 2 \frac{\partial S}{\partial x} \frac{\partial S}{\partial y} \frac{\partial^2 S}{\partial x \partial y} + \left(1 + \left(\frac{\partial S}{\partial y}\right)^2\right) \frac{\partial^2 S}{\partial x^2}}{\left(1 + \left(\frac{\partial S}{\partial x}\right)^2 + \left(\frac{\partial S}{\partial y}\right)^2\right)^{\frac{3}{2}}} \quad (7)$$

for bathymetry data defined by $z = S(x,y)$. Figure 11a shows the sea floor depth over the area studied, and Figure 11b shows a cross section from west to east over the area. The sea floor is approximately bowl shaped over the Ekofisk reservoir, and the lowest point occurs at the approximate

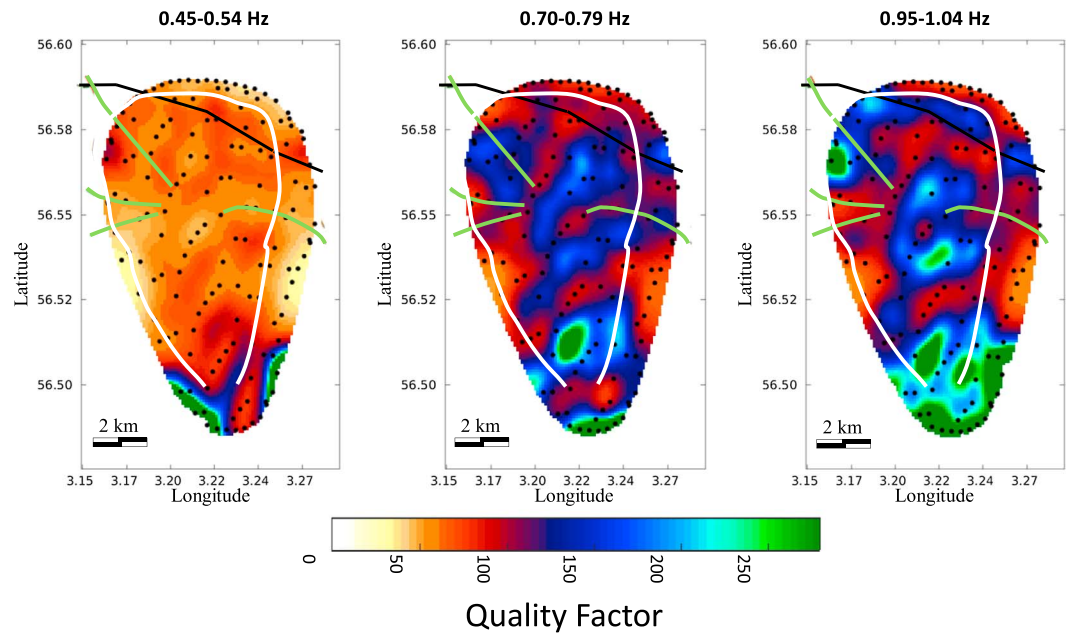


Figure 10. Quality factor Q results with position of known fault marked (black line in north of the array). In addition, the subsurface outline of the reservoir has been marked in white. The other lines (green) are pipelines. The fault corresponds to the linear feature of high-quality factor in the north of the array. To the north of the fault Q values are high, while to the south of the array Q values are low (fault and pipeline location from FactMaps, Norwegian Petroleum Directorate).

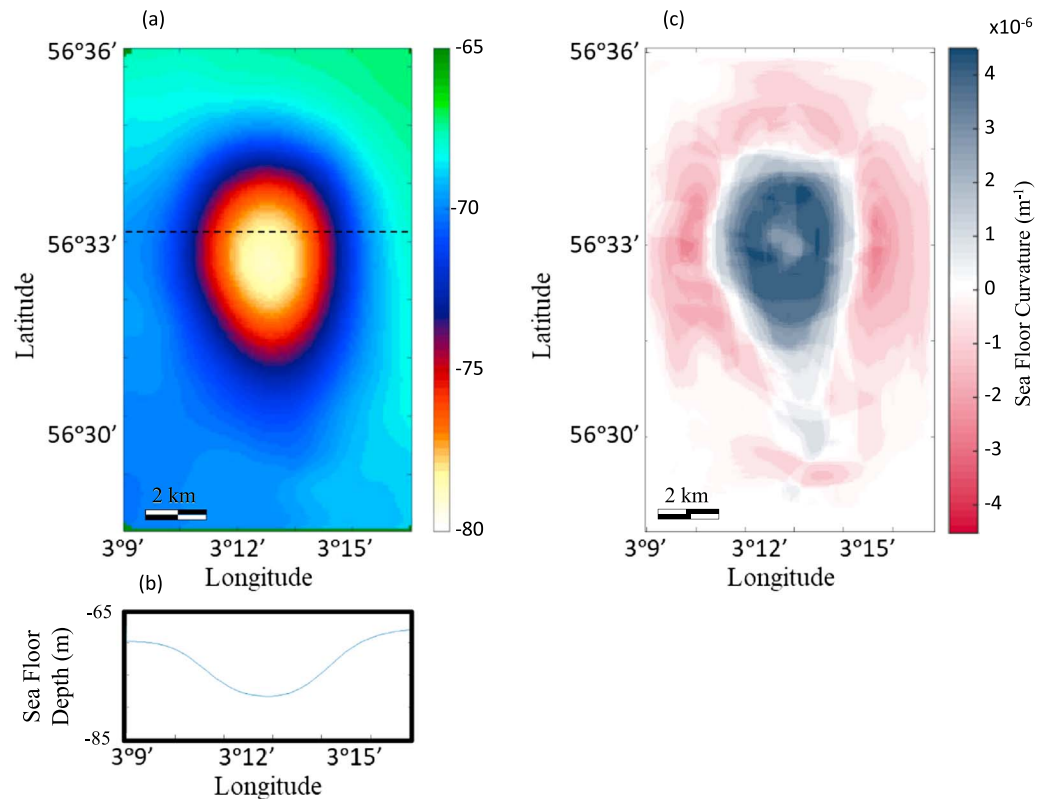


Figure 11. (a) Sea floor depth for the area of study. The sea floor is approximately bowl shaped, dipping to its lowest point at the platform. (b) A cross section of the sea floor depth at the location of the black dashed line in (a). (c) Sea floor mean curvature. There is positive curvature within the bowl and negative curvature on the lip.

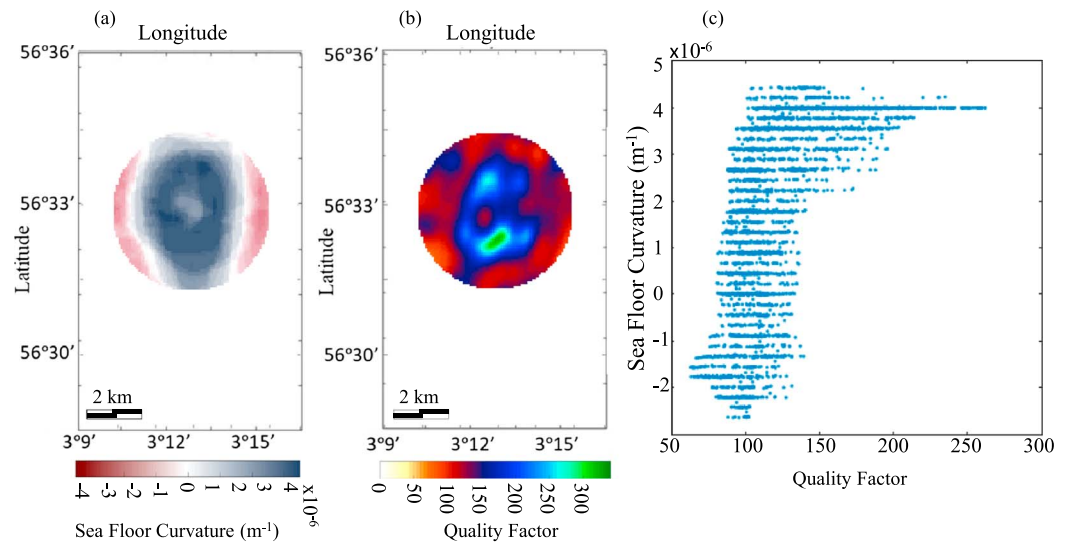


Figure 12. (a) Sea floor curvature within the bowl of subsidence only. (b) Q within the bowl of subsidence only. (c) Sea floor curvature plotted against quality factor for the circular areas shown in (a) and (b). There is a clear gradual increase in average Q value with curvature, with a strong increase in Q at large curvature.

location of the platform. Figure 11c shows the mean curvature of the sea floor. There is positive curvature within the bowl and negative curvature on the lip.

We compare the sea floor curvature with the Q structure within the area of the ring of high Q . Figures 12a and 12b show the sea floor curvature and Q within this circular area only. Figure 12c cross-plots the sea floor curvature against Q . This plot shows that where there is high positive curvature which is where there may be compression of the sea floor, high Q values are observed. At lower and negative curvature, Q increases more gradually with curvature. So compression of the sea floor appears to give higher Q values, possibly due to

compressional closing of fractures at the sea floor. This relation between compression and fracture closure has also been suggested by Nagel (2001), who show in their Figure 7 a compressional zone in the center of the Ekofisk subsidence bowl and a tensional zone on the lip of the subsidence bowl, and also by de Ridder and Biondi (2015a), who saw related effects on the seismic velocities.

Figure 13 shows an example, using a sine shaped topographic displacement, of how compression and dilation occur due to subsidence. The plot shows the normals to the sine curve at regular intervals. These diverge when they are on the outside of a bend in topographic displacement which occurs near the edges of the subsidence bowl (where curvature is negative), and converge when on the inside of a bend (where curvature is positive). It therefore seems plausible that the ring of increased Q compared to the background is caused by the closing of fractures in this part of the seabed. Johnston et al. (1979) state that under most conditions in the Earth's upper crust, friction on thin cracks and grain boundaries is the main source of attenuation in consolidated rocks and that increased compression decreases the number of cracks. This would agree with our interpretation that where there are likely to be fractures there is lower Q , and where there are fewer fractures or where the fractures have smaller widths there is higher Q . However, this does not explain why there are lower Q values in the very center of the array.

In the center of the array, the Q structure is similar to the reservoir compaction presented by Guilbot and Smith (2002). In their Figure 11 (reproduced

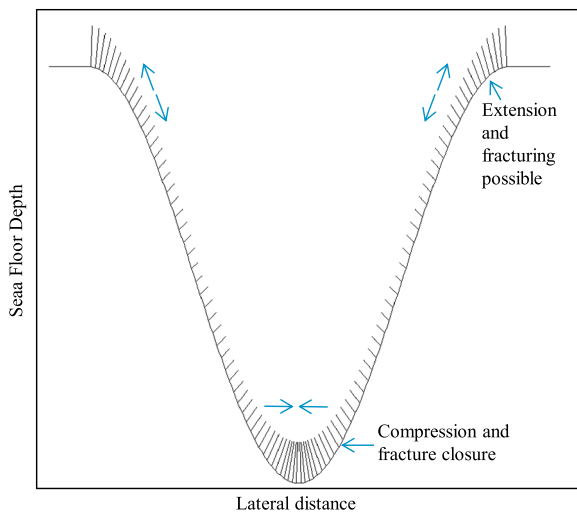


Figure 13. Assuming a standard sine wave for topographic deformation, a model of where there is compression and where there is dilation (fracturing) of material around a surface when bending (subsidence) occurs. The sine curve represents the seabed, and normals to the curve are shown. Toward the outer edges of the subsidence there is potential for fracturing where the rock is extended (diverging arrows), while at the base of the bowl there is compression where the rock is pushed together (converging arrows).

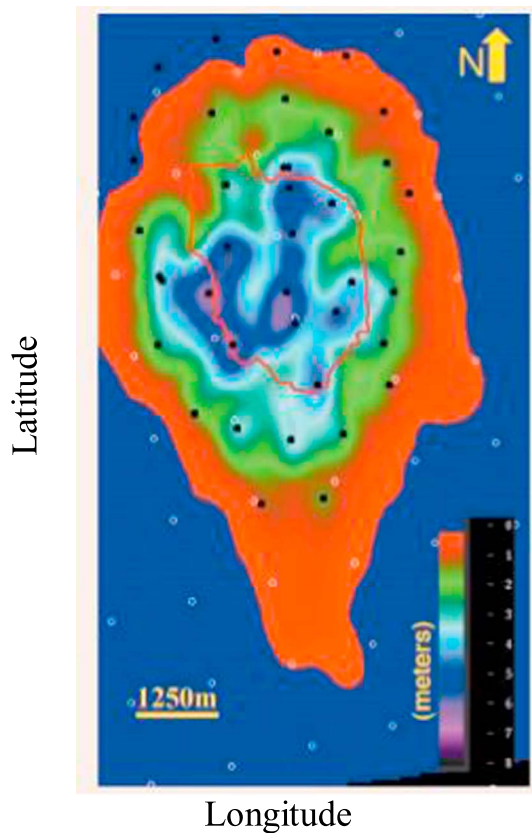


Figure 14. Compaction estimated using geomechanical modeling. Water injection wells are shown by black dots. This is Figure 11 of Guilbot and Smith (2002).

here in Figure 14) they present an estimate of the reservoir compaction at Ekofisk from geomechanical modeling. Their result has a high compaction structure which is ring-like in the center of the field, and compaction reduces with distance from the center. They also show a central area, within the ring of high compaction, with lower compaction. Their results fitted well with their seismically derived compaction map (which does not show the center of the array due to there being a seismically obscured area in the center of the array). The ringed structure of the velocity and Q at the Ekofisk array can also be observed in surface wave group velocity tomography (de Ridder et al., 2015; de Ridder & Biondi, 2015a), surface wave phase velocity tomography (de Ridder & Biondi, 2015b; de Ridder & Curtis, 2017), and compressional and shear wave velocity (Kazinnik et al., 2014) estimates at the site.

We therefore see that although our results cannot be explained by the compression and dilation of the seabed in the very center of the array, the ring of high Q surrounding the area of low Q is similar to patterns observed for other measurements made at the field. It may be that as the area of low Q is approximately at the platform location, the influence of the platform infrastructure and pipes could have caused fracturing to occur and hence a corresponding reduction in Q . The extensive drilling at the location of the platform will have caused some damage to the subsurface structure, and while drilling these wells there may have been an addition of fluid to the surrounding subsurface, either of which can cause a reduction in Q . The results around the platform location may therefore indicate the lateral extent of influence of the wells on subsurface structure. If the low Q at the center is due to the platform infrastructure, we would expect the effects to be observed at all depths to which drilling took place. In our results there is a value of Q in the center which is lower than the Q values immediately around that zone at all frequencies, and so if this is due to drilling, the effect can indeed be seen at all depth ranges considered here.

Another consideration is the similarity between the Q structure estimated and the compaction structure presented by Guilbot and Smith (2002). Their result shows that compaction at the center of the array is lower than in the ring around it; therefore, it could be that the lower Q values occur because compaction has not occurred at those locations to the same degree as in the ring around that area. The curvature of the seafloor presented in Figure 11 also has a ring in the center where the curvature is less than in the surrounding region. The curvature decrease at the center can therefore also be related to the Q structure. However, Doornhof et al. (2006) also present compaction at the Ekofisk field, and their result does not show a ring similar to that of Guilbot and Smith (2002). In the result presented in Doornhof et al. (2006) compaction increases toward the center of the Ekofisk array which could suggest that the most likely cause of the lower Q values in the center is due to the platform infrastructure. The interpretation of Q in this central area therefore remains enigmatic at this point in time. In section 6 we investigate why this ring is more apparent in the higher frequency results than at the two lower frequencies.

Conceptual models would suggest that due to increased pressure with depth, Q would also increase with depth due to crack closure. By contrast, our results show that Q is actually lower at the greatest depth considered (lowest frequency). There are of course other factors than simply fractures which affect Q , and hence, for example, a low Q layer at depths to which 0.5 Hz waves are sensitive could cause the decrease in Q with depth observed here.

6. Depth Sensitivity Analysis

In order to estimate the depth ranges which influence each of the three analyzed frequencies, a sensitivity analysis was carried out. The sensitivity analysis requires a model of S wave velocity with depth, which we

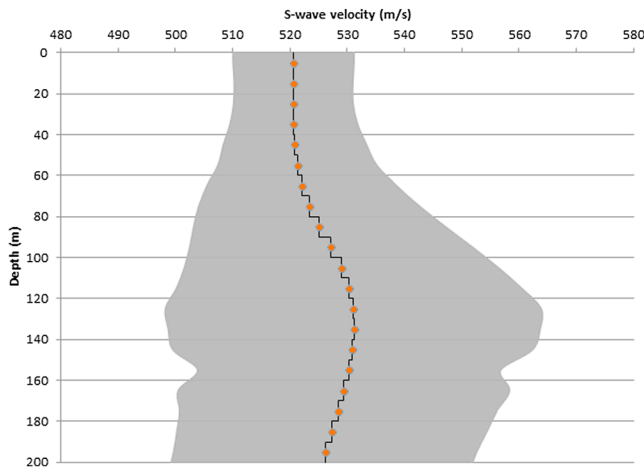


Figure 15. S wave velocity model used to estimate the sensitivity of phase velocity to shear velocity at different depths. Each orange circle represents a Voronoi nucleus, and the layers are marked by the dark horizontal lines. Each layer boundary is equidistant between the two neighboring Voronoi nodes. The gray shaded area shows the estimated uncertainty in the velocity model. This is the standard deviation of all the models averaged over to estimate the S wave velocity model.

estimated using a reversible-jump Markov chain Monte Carlo depth inversion of the phase velocities estimated for a single point that is roughly halfway between the edge and the center of the array as shown in Figure 5b.

6.1. Depth Inversion

The depth inversion code was an adaption of the original code of Bodin et al. (2012). The code was altered to use an alternative forward modeler (Surface Wave Modal Inversion [SWAMI]; Rix and Lai (2004)) which is better suited to shallow environments compared to the original forward modeler. In this inversion the Earth model is described by flat layers defined by Voronoi nuclei such that layer boundaries are equidistant between adjacent nuclei and the lowest layer is a half space (see Figure 15). Each layer is assigned a constant velocity value. During the inversion the positions and numbers of Voronoi nuclei are variable, as are the velocities associated with each layer. This means that the parametrization will adjust to suit the velocity structure information provided by the data during the inversion (Bodin et al., 2012).

In order to carry out the inversion, we begin with a random model \mathbf{m} described as above using Voronoi nuclei. We use a Bayesian formulation so that all information is represented in probabilistic terms. The aim of a Bayesian method is to quantify the a posteriori probability

distribution, which is the probability of obtaining each model \mathbf{m} given the observed data \mathbf{d}_{obs} , $p(\mathbf{m}|\mathbf{d}_{\text{obs}})$. For our initial starting model a likelihood function is defined, which describes the probability of obtaining the observed data from the current model $p(\mathbf{d}_{\text{obs}}|\mathbf{m})$. The model fit in this case is estimated using the SWAMI dispersion curve modeling code (Rix & Lai, 2004). A random perturbation is then made to the model \mathbf{m} to give a model \mathbf{m}' , and the likelihood of this model is calculated. A decision is made to either accept this new model or reject it randomly using an acceptance ratio criterion (Bodin et al., 2012). If the model is rejected, a new \mathbf{m}' is proposed. If the model is accepted, model \mathbf{m}' becomes our model \mathbf{m} and it is to this model that we make the next perturbation.

The acceptance ratio criterion is designed such that perturbations improve the data fit on average. In some cases the new model will not improve the fit to the data but the model will still be accepted. These types of moves are decided in a random fashion: If the acceptance ratio is greater than a random number between 0 and 1, the move will be accepted; if it is lower it will not. The application of the particular acceptance ratio employed means that samples will be generated according to the posterior probability distribution. This acceptance ratio is defined as

$$\alpha(\mathbf{m}'|\mathbf{m}) = \min \left[1, \frac{p(\mathbf{m}')}{p(\mathbf{m})} \times \frac{p(\mathbf{d}_{\text{obs}}|\mathbf{m}')}{p(\mathbf{d}_{\text{obs}}|\mathbf{m})} \times \frac{p(\mathbf{m}|\mathbf{m}')}{p(\mathbf{m}'|\mathbf{m})} \times |\mathbf{J}| \right] \quad (8)$$

in which $\frac{p(\mathbf{m}')}{p(\mathbf{m})}$ is the prior ratio in which the prior probability $p(\mathbf{m})$ describes what is known about the model parameters \mathbf{m} before applying the data \mathbf{d} , $\frac{p(\mathbf{d}_{\text{obs}}|\mathbf{m}')}{p(\mathbf{d}_{\text{obs}}|\mathbf{m})}$ is the likelihood ratio, $\frac{p(\mathbf{m}|\mathbf{m}')}{p(\mathbf{m}'|\mathbf{m})}$ is the proposal ratio with the proposal distribution $p(\mathbf{m}'|\mathbf{m})$ describing the probability of moving from model \mathbf{m} to model \mathbf{m}' , and \mathbf{J} is the Jacobian of the transformation from \mathbf{m} to \mathbf{m}' . The Jacobian accounts for scale changes involved when there is a change in dimension (the number of layers) and prevents unnecessary growth in the number of model parameters. The acceptance ratio is a Bayesian quantity which promotes natural parsimony, meaning that if \mathbf{m} and \mathbf{m}' are identical in all but the number of parameters then the model with the fewest parameters will be chosen and ensures that samples are distributed according to the posterior probability density (Galetti & Curtis, 2018). This algorithm generates samples according the posterior probability density (Galetti et al., 2016) and does so in an ordered chain.

Prior probabilities in velocity were uniform between 10 and 1,990 m/s. The likelihood function used corresponded to Gaussian data uncertainties. The above sampling process is repeated for 2.5 million models to

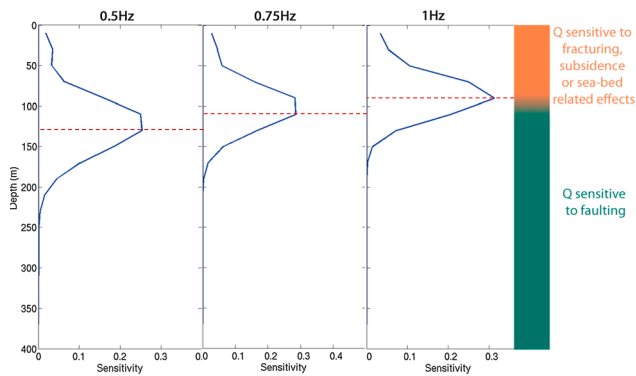


Figure 16. Sensitivity kernels for the three frequencies of analysis assuming the velocity model in Figure 15. The depth of maximum sensitivity increases with decreased frequency. We interpret that the results at 1 Hz are sensitive to fracturing, subsidence, and seabed-related effects, while the lower frequencies are more sensitive to faulting.

form a Markov chain. Sixteen Markov chains are calculated to give a large number of possible models. The samples in these chains are distributed according to the posterior distribution and form the solution to the inverse problem (Bodin et al., 2012). The posterior distribution describes how our knowledge has been improved from the prior knowledge by application of the data. The first 500,000 models of each chain are discarded thus removing any correlation with the random starting model. Then a subset of the remaining models is averaged to produce an estimate of the *S* wave velocity structure. The subset is chosen by taking every 100th model in the chain which removes the correlation between consecutive models. The resulting velocity structure estimated for Ekofisk is shown in Figure 15. Uncertainty in the *S* wave velocity model is also shown. The uncertainty is estimated by taking the standard deviation of all of the models over which we average.

In our application of the method we input phase velocity dispersion curves estimated from the phase velocity maps. A single location is chosen within the receiver array (Figure 5b), and the phase velocities estimated for a set of frequencies at that location are used to define the dispersion curve. The above method is then applied to estimate the *S* wave velocity profile beneath that location. *S* wave velocity profiles will not be identical over the array, and so the sensitivity kernels estimated below are approximate, giving only an indication of the possible depth ranges for each frequency.

6.2. Sensitivity Analysis

Following the estimation of the reference *S* wave velocity profile at Ekofisk, a sensitivity analysis was carried out by estimating the phase velocity dispersion curve (again using the SWAMI code) for the reference velocity model before applying a small perturbation at each depth in turn. After applying a small perturbation to a single depth, the dispersion curve was again estimated and the difference between the two curves at each frequency was calculated. This difference was divided by the perturbation to give an estimate of the derivative of the phase velocity with respect to the shear velocity at each depth (which is called the sensitivity function). We assume that the sensitivity of *Q* follows that of the phase velocity as these two parameters are linked through equation (4).

Sensitivity kernels are shown in Figure 16 for the three analyzed frequencies. Depths of maximum sensitivity for 0.5, 0.75, and 1 Hz are 130, 110, and 90 m, respectively. This follows the typical pattern of increased depth of sensitivity with decreased frequency.

Our interpretation of the results is that between approximately 0 and 100 m there is a ring of low *Q* where the topography in Figure 11b has negative curvature, and this is sampled by the 1-Hz waves. It also appears at 0.75 Hz but with a lower amplitude anomaly. For frequencies of 0.5 Hz and lower the sensitivity increases to 130 m and below, and we see that *Q* is not dominated by the effects of curvature. Instead, we observe a pattern which shows some relation to faulting (Figure 10).

Hence, shallow subsurface *Q* is particularly sensitive to the effects of the seabed. This may be due to the increased range in fracture aperture that is possible in regimes of low compressive stress, to increased porosity and hence volume of (shear-stress free) water in the near seabed rock volume, or (since Scholte waves are very sensitive to shear velocity in the solid medium) simply to the existence of the seabed across which shear stress is 0. All three of these effects on *Q* would decrease for deeper rocks that are further away from the seabed, hence the decrease in seabed structure influence at deeper depths (lower frequencies) that we observe.

7. Discussion

7.1. Quality Factor Versus Site Amplification

One of the assumptions made in this analysis was that we could consider the site amplification to be approximately equal across the full extent of the array. This may not be valid, and it may be that we are actually

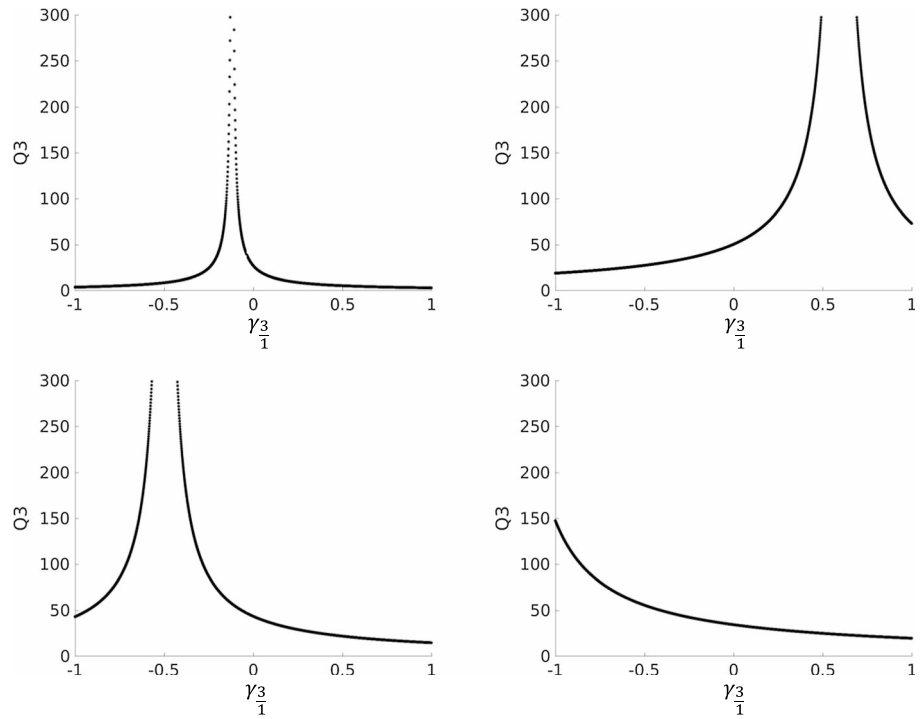


Figure 17. Comparison of Q_3 values estimated with different site amplification ($\gamma_{\frac{3}{1}}$) for four example receiver triplets in the Ekofisk array. Each curve represents the range of possible Q_3 values which we could estimate for a single triplet when considering different $\gamma_{\frac{3}{1}}$ values. There is a strong influence on Q_3 from the site amplification.

observing the pattern of the relative site amplifications at the receivers rather than the Q structure, or a combination of both. Rearranging equation (4) gives

$$Q_3 \left(1 - \frac{\gamma_{\frac{3}{1}}}{\ln \hat{C}_{u_2 u_3}^+(\omega) - \ln \hat{C}_{u_1 u_2}^+(\omega)} \right) = \frac{-\omega x_3}{2c_3 (\ln \hat{C}_{u_2 u_3}^+(\omega) - \ln \hat{C}_{u_1 u_2}^+(\omega))} \quad (9)$$

where the right-hand side of equation (9) is a known constant for each receiver triplet. By using equation (9) to plot Q_3 against $\gamma_{\frac{3}{1}}$ for different receiver triplets, we investigate the effect of assuming that γ values are equal over the array.

When we assume that gamma is equal to 0, we choose to restrict our analysis to one of the points on each of the curves shown in Figure 17 for the four example triplets shown, which may not be correct. In the figure, Q is shown to extend over a range of values dependent on the local site amplification, which in some instances causes Q to tend to infinity; at such points Q^{-1} (attenuation) tends to 0, which is not unrealistic. If Q^{-1} is averaged for thousands of paths, as we do for this work, then the perturbations to Q^{-1} caused by the site amplification factors differing over the different receiver triplets will cancel out to a significant extent. Hence, averaged Q_3^{-1} estimates should be relatively stable and still reflect the attenuation structure, even with unknown site amplification.

Differences in site amplification factors over the array will exist in reality, but as the problem is underdetermined the data only provides a constraint on the curve which exists for each triplet and not which point of the curve should be used. The plots in Figure 17 show that the site amplification factors can make a substantial difference to the Q values estimated. These curves therefore define the residual nonuniqueness in the solution to our problem. However, the receiver type over the Ekofisk array is homogeneous and data acquisition teams aim to minimize the differences between receivers. So although the local geology and receiver coupling will not be equal across the array, we can hope that the site amplification differences are small enough that our assumption is not too unrealistic. The sensitivity function of the sensors themselves is

Table 1
Approximate Energy Loss at 1, 0.5, and 0.1 Hz for Waves Traveling Across the North Sea From Norway to the British Isles if Q Values Are Comparable to Those at Ekofisk Over the Area of the North Sea

		1 Hz	0.5 Hz	0.1 Hz
Approximate velocity		0.42 km/s	0.49 km/s	0.47 km/s
Approximate wavelength		0.42 km	0.98 km	4.7 km
Approximate number of wavelengths to cross North Sea		1,548	663	138
Approximate energy remaining in signal after crossing North Sea when initial energy = 1	Q = 75	1.5×10^{-59}	6.4×10^{-26}	5.7×10^{-06}
	Q = 150	1.7×10^{-29}	4.8×10^{-13}	2.7×10^{-03}

approximately the same for all sensors in the Ekofisk array. Although the local geology is heterogeneous, the top few meters are of fairly homogeneous sedimentary cover, and the cables are trenched into the seabed. Therefore, we expect the site amplification factors to be similar for all stations. Although we have assumed equal site amplification over the Ekofisk array, it would be interesting to investigate the effect of including site amplification estimates on the Q estimate. In order to estimate site amplification factors further, independent data would be required. For example, it may be possible to estimate site amplification by firing impulsive shots above and to the side of each receiver and measuring the first response from the direct down going waves. However, one would have to ensure that such a site amplification estimated was appropriate to be used in this current method of estimating Q , so further research would be needed to assess this.

7.2. Nonlinear Relationship Between Q and Compression

In Figure 12c we observe a significantly nonlinear relationship between curvature of the seabed and Q . For all small curvatures there is a gradual increase in average Q values with curvature, but a strong increase in Q occurs at large positive curvature. Since compressive horizontal stress must be associated with positive curvatures by Figure 13, it appears that Q relates nonlinearly to compressive stress.

The relationship between curvature and fracture density is well known (e.g., Hunt et al., 2009; Jolley, 2007; Suo et al., 2012). When a rock is brittle and failure results in fracturing, any increase in magnitude of negative curvature resulting in an increase in strain will cause an increase in fracture density (Hunt et al., 2009). The increased attenuation due to fractures has also been studied (Rodríguez-Pradilla, 2015; Rubino et al., 2014; Watanabe & Sassa, 1996); hence, it is unsurprising that there is also a relationship between curvature and Q . Nevertheless, the particular form of the relationship that we find in Figure 12 is new and may be useful for further studies.

7.3. North Sea Ambient Noise Propagation

Nicolson et al. (2014) and Galetti et al. (2016) found that when applying ambient noise interferometry to noise collected at receivers on opposite sides of the central North Sea (data collected in the UK and in Norway) the cross correlations produced noticeably unreliable virtual source seismograms at periods of 1 to 10 s. This may be explained by the Q values estimated for the Ekofisk array. If these values can be considered to be similar to those across large areas of the North Sea, we find that the attenuation is too great for signals to emerge with a virtual source in Norway and a receiver in the British Isles. This is best explained by a numerical example.

The distances between receivers in Norway and on the British Isles range between about 500 and 750 km, and so for this example we consider a trans-North Sea distance of 650 km. From equation (1) we can estimate the energy loss per unit cycle if we know the initial energy in the signal and the Q value. Table 1 gives examples of the energy remaining in a signal at three frequencies (1, 0.5, and 0.1 Hz) for waves which traverse the North Sea from Norway to the British Isles, based on the initial energy having amplitude of 1 and Q being constant over the area traversed. The table clearly shows that waves lose most of their energy with Q values equal to 75 and 150 (typical values found in this study) when traversing the North Sea. This explains the poor recovery of signals from ambient noise interferometry between receiver pairs spanning this area within the period range of 1 to 2 s. At other periods it may be that the virtual seismograms are more reliable.

For coherent energy to be recorded at different receivers it should come from the same source. Consider the case where the two receivers are on opposite sides of the North Sea. As the energy from the sources cannot

propagate across the North Sea without undergoing attenuation to negligible amplitude, there are no common sources for the two receivers. Therefore, local ambient noise at one or other receivers will be recorded, together with any small remaining energy that is common to both receivers. The coherent energy from common sources is dominated by the incoherent energy from the local sources due to the attenuated amplitudes, thus causing the cross correlations to be incoherent.

8. Conclusions

By implementing the methods of Bloch and Hales (1968) and X. Liu et al. (2015), we present both phase velocity and Q tomography at the Ekofisk field. We show that although phase velocity is required for the estimation of Q there is little or no correlation between these two parameters, which means that the Q results are not dominated by our estimates of phase velocities. We also show that there is some continuity in the Q structure and phase velocity structure across different frequencies and therefore depth ranges.

Some of the observed Q structures can be related to known geological features at the Ekofisk field. There is a linear zone of high Q in the north of the array, the position of which roughly corresponds to the location of a known fault. At 1 Hz and in the east of the Q results for 0.5 and 0.75 Hz this fault separates an area with a high Q value from an area with a low Q value. A high Q ring in the center of the Q maps has been related to the sea floor subsidence which is known to have taken place at the Ekofisk field; however, this cannot explain the lower Q values in the very center of the array. Where there is large positive curvature of the seabed there is high Q : This is where there is compression of the seabed which will reduce fracture widths. Q is known to be reduced by the presence of fractures, and so by reducing fracture widths there is a natural increase in Q . The results show that in the circular area of the array compression due to subsidence-related seafloor curvature causes increased Q . What is more, this relationship was observed to be significantly nonlinear with a sharp increase in Q for the largest curvatures encountered.

Our results also explain the poor signal-to-noise ratio in ambient noise interferometry-derived signals by Nicolson et al. (2014) and Galetti et al. (2016) for signals crossing the North Sea. If the Q values we observe are representative across the North Sea basin, then all ambient noise traversing from one side of the sea to the other will be attenuated to nearly 0.

Acknowledgments

The authors thank the Edinburgh Interferometry Project sponsors (Schlumberger Gould Research, Statoil, ConocoPhillips, and Total) for supporting this research. The data for this manuscript may be requested from the Ekofisk project partners Petoro (<https://www.petoro.no>), Statoil (<https://www.statoil.com>), ENI (<https://www.eni.com>), ConocoPhillips (<https://www.conocophillips.com/>), or Total (<https://www.total.com/en>). The authors also thank the reviewers for their thoughtful and constructive comments which improved the quality of this manuscript.

References

- Aki, K. (1980). Scattering and attenuation of shear waves in the lithosphere. *Journal of Geophysical Research*, 85(B11), 6496–6504. <https://doi.org/10.1029/JB085iB11p06496>
- Aki, K., & Richards, P. G. (1980). *Quantitative seismology*. Sausalito, CA: University Science Books.
- Allen, T. I., Cummins, P. R., Dhu, T., & Schneider, J. F. (2007). Attenuation of ground-motion spectral amplitudes in southeastern Australia. *Bulletin of the Seismological Society of America*, 97(4), 1279–1292. <https://doi.org/10.1785/0120060172>
- Barkved, O. I., Kristiansen, T., & Fjaer, E. (2005). The 4D seismic response of a compacting reservoir—examples from the Valhall Field, Norway. In *SEG Technical Program Expanded Abstracts 2005. 1 January 2005, Society of Exploration Geophysicists* (pp. 2508–2511).
- Beckwith, J., Clark, R., & Hodgson, L. (2016). Estimating frequency-dependent attenuation quality factor values from prestack surface seismic data. *Geophysics*, 82(1), O11–O22.
- Bensen, G. D., Ritzwoller, M. H., Barmin, M. P., Levshin, A. L., Lin, F., Moschetti, M. P., et al. (2007). Processing seismic ambient noise data to obtain reliable broad-band surface wave dispersion measurements. *Geophysical Journal International*, 169(3), 1239–1260. <https://doi.org/10.1111/j.1365-246X.2007.03374.x>
- Bertrand, A., Buizard, S., & Grandi, A. (2014). Ekofisk life-of-field seismic: Operations and 4D processing. *The Leading Edge*, 33(2), 142–148. <https://doi.org/10.1190/tle33020142.1>
- Bhattacharya, S. (1983). Higher order accuracy in multiple filter technique. *Bulletin of the Seismological Society of America*, 73(5), 1395–1406.
- Bloch, S., & Hales, A. L. (1968). New technique for the determination of surface wave phase velocities. *Bulletin of the Seismological Society of America*, 58(3), 1021–1034. Retrieved from <https://pubs.geoscienceworld.org/ssa/bssa/article-abstract/58/3/1021/116607>
- Bodin, T., Sambridge, M., Tkalcic, H., Arroucau, P., Gallagher, K., & Rawlinson, N. (2012). Transdimensional inversion of receiver functions and surface wave dispersion. *Journal of Geophysical Research*, 117, B02301. <https://doi.org/10.1029/2011JB008560>
- Buizard, S., Bertrand, A., Nielsen, K.M., de Pierrepont, S., Grandi, A., Hoerber, H., et al. (2013). Ekofisk Life of Field Seismic—4D processing. In *75th EAGE Conference & Exhibition incorporating SPE EUROPEC 2013*. 10 June 2013.
- Carcione, J. M. (2000). A model for seismic velocity and attenuation in petroleum source rocks. *Geophysics*, 65(4), 1080–1092. <https://doi.org/10.1190/1.1444801>
- Chapman, M., Liu, E., & Li, X.-Y. (2006). The influence of fluid-sensitive dispersion and attenuation on AVO analysis. *Geophysical Journal International*, 167(1), 89–105. <https://doi.org/10.1111/j.1365-246X.2006.02919.x>
- Curtis, A., Gerstoft, P., Sato, H., Snieder, R., & Wapenaar, K. (2006). Seismic interferometry—Turning noise into signal. *The Leading Edge*, 25(9), 1082–1092. <https://doi.org/10.1190/1.2349814>
- Dasgupta, R., & Clark, R. A. (1998). Estimation of Q from surface seismic reflection data. *Geophysics*, 63(6), 2120–2128. <https://doi.org/10.1190/1.1444505>
- Dasios, A., Astin, T. R., & McCann, C. (2001). Compressional-wave Q estimation from full-waveform sonic data. *Geophysical Prospecting*, 49(3), 353–373. <https://doi.org/10.1046/j.1365-2478.2001.00259.x>

- de Ridder, S. A. L., & Biondi, B. L. (2015a). Ambient seismic noise tomography at Ekofisk. *Geophysics*, *80*(6), B167–B176. <https://doi.org/10.1190/geo2014-0558.1>
- de Ridder, S. A. L., & Biondi, B. L. (2015b). Near-surface Scholte wave velocities at Ekofisk from short noise recordings by seismic noise gradiometry. *Geophysical Research Letters*, *42*, 7031–7038. <https://doi.org/10.1002/2015GL065027>
- de Ridder, S. A. L., Biondi, B. L., & Nichols, D. (2015). Elliptical-anisotropic eikonal phase velocity tomography. *Geophysical Research Letters*, *42*, 758–764. <https://doi.org/10.1002/2014GL062805>
- de Ridder, S. A. L., & Curtis, A. (2017). Seismic gradiometry using ambient seismic noise in an anisotropic Earth. *Geophysical Journal International*, *176*(1), 198–212.
- Doornhof, D., TG Kristiansen, T. B., Neal Nagel, N. B., Pattillo, P. D., Sayers, C., Barkved, O., et al. (2006). Compaction and subsidence. *Oilfield Review*, *18*(3), 50–68.
- Dvorkin, J. P., & Mavko, G. (2006). Modeling attenuation in reservoir and nonreservoir rock. *The Leading Edge*, *25*(2), 194–197. <https://doi.org/10.1190/1.2172312>
- Dziewonski, A., Bloch, S., & Landisman, M. (1969). A technique for the analysis of transient seismic signals. *Bulletin of the Seismological Society of America*, *5*(111), 427–444.
- Ekanem, A. M., Wei, J., Li, X.-Y., Chapman, M., & Main, I. G. (2013). P-wave attenuation anisotropy in fractured media: A seismic physical modelling study. *Geophysical Prospecting*, *61*(s1), 420–433. <https://doi.org/10.1111/j.1365-2478.2012.01127.x>
- Fehler, M., Hoshihara, M., Sato, H., & Obara, K. (1992). Separation of scattering and intrinsic attenuation for the Kanto-Tokai region, Japan, using measurements of S-wave energy versus hypocentral distance. *Geophysical Journal International*, *108*(3), 787–800. <https://doi.org/10.1111/j.1365-246X.1992.tb03470.x>
- Frankel, A., & Wennnerberg, L. (1987). Energy-flux model of seismic coda: Separation of scattering and intrinsic attenuation. *Bulletin of the Seismological Society of America*, *77*(4), 1223–1251.
- Galetti, E., & Curtis, A. (2018). Transdimensional electrical resistivity tomography. *Journal of Geophysical Research: Solid Earth*, *123*. <https://doi.org/10.1029/2017JB015418>
- Galetti, E., Curtis, A., Baptie, B., Jenkins, D., & Nicolson, H. (2016). Transdimensional love-wave tomography of the British Isles and shear-velocity structure of the east Irish Sea basin from ambient-noise interferometry. *Geophysical Journal International*, ggw286.
- Gei, D., & Carcione, J. M. (2003). Acoustic properties of sediments saturated with gas hydrate, free gas and water. *Geophysical Prospecting*, *51*(2), 141–158. <https://doi.org/10.1046/j.1365-2478.2003.00359.x>
- Gennaro, M., Wonham, J. P., Saalen, G., Walgenwitz, F., Caline, B., & Fay-Gomord, O. (2013). Characterization of dense zones within the Danian chalks of the Ekofisk field, Norwegian North Sea. *Petroleum Geoscience*, *19*(1), 39–64. <https://doi.org/10.1144/pet-geo2012-013>
- Goldman, R. (2005). Curvature formulas for implicit curves and surfaces. *Computer Aided Geometric Design*, *22*(7), 632–658. <https://doi.org/10.1016/j.cagd.2005.06.005>
- Gouédard, P., Stehly, L., Brenguier, F., Campillo, M., Colin de Verdière, Y., Larose, E., et al. (2008). Cross-correlation of random fields: Mathematical approach and applications. *Geophysical Prospecting*, *56*(3), 375–393. <https://doi.org/10.1111/j.1365-2478.2007.00684.x>
- Guilbot, J., & Smith, B. (2002). 4-D constrained depth conversion for reservoir compaction estimation: Application to Ekofisk field. *The Leading Edge*, *21*(3), 302–308. <https://doi.org/10.1190/1.1463782>
- Halliday, D., & Curtis, A. (2008). Seismic interferometry, surface waves and source distribution. *Geophysical Journal International*, *175*(3), 1067–1087. <https://doi.org/10.1111/j.1365-246X.2008.03918.x>
- Halliday, D., & Curtis, A. (2009). Seismic interferometry of scattered surface waves in attenuative media. *Geophysical Journal International*, *178*(1), 419–446. <https://doi.org/10.1111/j.1365-246X.2009.04153.x>
- Hunt, L., Chopra, S., Reynolds, S., & Hadley, S. (2009). On calibrating curvature data to fracture density: Causes. *CSEG Recorder*, *34* (10).
- Johnston, D. H., Toksöz, M. N., & Timur, A. (1979). Attenuation of seismic waves in dry and saturated rocks: II. Mechanisms. *Geophysics*, *44*(4), 691–711. <https://doi.org/10.1190/1.1440970>
- Jolley, S. J. (2007). *Structurally complex reservoirs*. London: Geological Society.
- Joshi, A. (2007). Inversion of seismic intensity data for the determination of three-dimensional attenuation structures in the central gap region of Himalayas. *Natural Hazards*, *43*(1), 1–22. <https://doi.org/10.1007/s11069-006-9098-6>
- Kazinnik, R., Roy, B., Tura, A., Vedvik, L., & Knoth, O. (2014). Near surface velocities at Ekofisk from Scholte and refracted wave analysis. In *SEG Technical Program Expanded Abstracts 2014. 5 August 2014, Society of Exploration Geophysicists* (pp. 2036–2039).
- Lawrence, J. F., & Prieto, G. A. (2011). Attenuation tomography of the western United States from ambient seismic noise. *Journal of Geophysical Research*, *116*, B06302. <https://doi.org/10.1029/2010JB007836>
- Li, H., Zhao, W., Cao, H., Yao, F., & Shao, L. (2006). Measures of scale based on the wavelet scalogram with applications to seismic attenuation. *Geophysics*, *71*(5), V111–V118. <https://doi.org/10.1190/1.2211529>
- Lin, F.-C., Ritzwoller, M. H., & Shen, W. (2011). On the reliability of attenuation measurements from ambient noise cross-correlations. *Geophysical Research Letters*, *38*, L11303. <https://doi.org/10.1029/2011GL047366>
- Lin, F.-C., Tsai, V. C., & Ritzwoller, M. H. (2012). The local amplification of surface waves: A new observable to constrain elastic velocities, density, and anelastic attenuation. *Journal of Geophysical Research*, *117*, B06302. <https://doi.org/10.1029/2012JB009208>
- Liu, E., Chapman, M., Varella, I., Li, X., Queen, J. H., & Lynn, H. (2007). Velocity and attenuation anisotropy: Implication of seismic fracture characterizations. *The Leading Edge*, *26*(9), 1170–1174. <https://doi.org/10.1190/1.2780788>
- Liu, X., Ben-Zion, Y., & Zigone, D. (2015). Extracting seismic attenuation coefficients from cross-correlations of ambient noise at linear triplets of stations. *Geophysical Journal International*, *203*(2), 1149–1163. <https://doi.org/10.1093/gji/ggv357>
- Maultzsch, S., Chapman, M., Liu, E., & Li, X.-Y. (2007). Modelling and analysis of attenuation anisotropy in multi-azimuth VSP data from the Clair field. *Geophysical Prospecting*, *55*(5), 627–642. <https://doi.org/10.1111/j.1365-2478.2007.00645.x>
- McNamara, D. E., Gee, L., Benz, H. M., & Chapman, M. (2014). Frequency-dependent seismic attenuation in the eastern United States as observed from the 2011 Central Virginia earthquake and aftershock sequence. *Bulletin of the Seismological Society of America*, *104*(1), 55–72. <https://doi.org/10.1785/0120130045>
- Morton, S., Peterie, S., Ivanov, J., Miller, R., Feigenbaum, D., Sloan, S., et al. (2016). Feasibility study using surface wave attenuation and seismic quality factor for tunnel detection at the Yuma proving ground, AZ : SEG Technical Program Expanded Abstracts: Vol. , No. (Society of Exploration Geophysicists). *SEG Technical Program Expanded Abstracts* (pp. 2351–2356).
- Nagel, N. B. (2001). Compaction and subsidence issues within the petroleum industry: From Wilmington to Ekofisk and beyond. *Physics and Chemistry of the Earth, Part A: Solid Earth and Geodesy*, *26*(1–2), 3–14. [https://doi.org/10.1016/S1464-1895\(01\)00015-1](https://doi.org/10.1016/S1464-1895(01)00015-1)
- Nicolson, H., Curtis, A., & Baptie, B. (2014). Rayleigh wave tomography of the British Isles from ambient seismic noise. *Geophysical Journal International*, *198*(2), 637–655. <https://doi.org/10.1093/gji/ggu071>

- Nicolson, H., Curtis, A., Baptie, B., & Galetti, E. (2012). Seismic interferometry and ambient noise tomography in the British Isles. *Proceedings of the Geologists Association*, 123(1), 74–86. <https://doi.org/10.1016/j.pgeola.2011.04.002>
- Oelze, M., Darmody, R., & O'Brien, W. (2001). Measurement of attenuation and speed of sound in soils for the purposes of imaging buried objects. *The Journal of the Acoustical Society of America*, 109(5), 2287–2287. <https://doi.org/10.1121/1.4744005>
- Ottmöller, L. (2005). The 7 May 2001 induced seismic event in the Ekofisk oil field, North Sea. *Journal of Geophysical Research*, 110, B10301. <https://doi.org/10.1029/2004JB003374>
- Parolai, S. (2014). Shear wave quality factor Q_s profiling using seismic noise data from microarrays. *Journal of Seismology*, 18(3), 695–704. <https://doi.org/10.1007/s10950-014-9440-5>
- Prasad, M., & Manghnani, M. H. (1997). Effects of pore and differential pressure on compressional wave velocity and quality factor in Berea and Michigan sandstones. *Geophysics*, 62(4), 1163–1176. <https://doi.org/10.1190/1.1444217>
- Pride, S. R., Berryman, J. G., & Harris, J. M. (2004). Seismic attenuation due to wave-induced flow. *Journal of Geophysical Research*, 109, B01201. <https://doi.org/10.1029/2003JB002639>
- Priest, J. A., Best, A. I., & Clayton, C. R. I. (2006). Attenuation of seismic waves in methane gas hydrate-bearing sand. *Geophysical Journal International*, 164(1), 149–159.
- Prieto, G. A., Denolle, M., Lawrence, J. F., & Beroza, G. C. (2011). On amplitude information carried by the ambient seismic field. *Comptes Rendus Geosciences*, 343(8–9), 600–614. <https://doi.org/10.1016/j.crte.2011.03.006>
- Quan, Y., & Harris, J. M. (1997). Seismic attenuation tomography using the frequency shift method. *Geophysics*, 62(3), 895–905. <https://doi.org/10.1190/1.1444197>
- Raghu Kanth, S. T. G., & Iyengar, R. N. (2007). Estimation of seismic spectral acceleration in peninsular India. *Journal of Earth System Science*, 116(3), 199–214. <https://doi.org/10.1007/s12040-007-0020-8>
- Rawlinson, N. (2005). Fast marching surface tomography. Research School of Earth Sciences, Australian National University.
- Rix, G. J., & Lai, C. G. (2004). SWAMI—Surface Wave Model Inversion.
- Rodríguez-Pradilla, G. (2015). Applications of shallow-seismic exploration methods for mechanical characterization of soil and rock bodies at engineering project sites in Colombia. *The Leading Edge*, 34(2), 166–168. <https://doi.org/10.1190/tle34020166.1>
- Rossi, G., Gei, D., Böhm, G., Madrussani, G., & Carcione, J. M. (2007). Attenuation tomography: An application to gas-hydrate and free-gas detection. *Geophysical Prospecting*, 55(5), 655–669. <https://doi.org/10.1111/j.1365-2478.2007.00646.x>
- Rubino, J. G., Müller, T. M., Guaracino, L., Milani, M., & Holliger, K. (2014). Seismoacoustic signatures of fracture connectivity. *Journal of Geophysical Research: Solid Earth*, 119, 2252–2271. <https://doi.org/10.1002/2013JB010567>
- Sain, K., Singh, A. K., Thakur, N. K., & Khanna, R. (2009). Seismic quality factor observations for gas-hydrate-bearing sediments on the western margin of India. *Marine Geophysical Researches*, 30(3), 137–145. <https://doi.org/10.1007/s11001-009-9073-1>
- Saygin, E., Cummins, P. R., Cipta, A., Hawkins, R., Pandhu, R., Murjaya, J., et al. (2015). Imaging architecture of the Jakarta Basin, Indonesia with transdimensional inversion of seismic noise. *Geophysical Journal International*, 204(2), 918–931.
- Shearer, P. M. (2009). *Introduction to seismology*. Cambridge, UK: Cambridge University Press. <https://doi.org/10.1017/CBO9780511841552>
- Singhroha, S., Bünz, S., Plaza-Faverola, A., & Chand, S. (2016). Gas hydrate and free gas detection using seismic quality factor estimates from high-resolution P-cable 3D seismic data. *Interpretation*, 4(1), SA39–SA54. <https://doi.org/10.1190/INT-2015-0023.1>
- Sniieder, R. (2004). Extracting the Green's function from the correlation of coda waves: A derivation based on stationary phase. *Physical Review E, Statistical, Nonlinear, and Soft Matter Physics*, 69(4 Pt 2), 46610.
- Sniieder, R., Wapenaar, K., & Larner, K. (2006). Spurious multiples in seismic interferometry of primaries. *Geophysics*, 71(4), S1111–S1124. <https://doi.org/10.1190/1.2211507>
- Suo, C., Peng, S., Chang, S., Duan, R., & Wang, G. (2012). A new calculating method of the curvature to predicting the reservoir fractures. *Procedia Environmental Sciences*, 12, 576–582. <https://doi.org/10.1016/j.proenv.2012.01.320>
- Watanabe, T., & Sassa, K. (1996). Seismic attenuation tomography and its application to rock mass evaluation. *International Journal of Rock Mechanics and Mining Science and Geomechanics Abstracts*, 33(5), 467–477. [https://doi.org/10.1016/0148-9062\(96\)00005-8](https://doi.org/10.1016/0148-9062(96)00005-8)
- Waters, K. R., Mobley, J., & Miller, J. G. (2005). Causality-imposed (Kramers-Kronig) relationships between attenuation and dispersion. *IEEE Transactions on Ultrasonics, Ferroelectrics, and Frequency Control*, 52(5), 822–823. <https://doi.org/10.1109/TUFFC.2005.1503968>
- Xia, J. (2014). Estimation of near-surface shear-wave velocities and quality factors using multichannel analysis of surface-wave methods. *Journal of Applied Geophysics*, 103, 140–151. <https://doi.org/10.1016/j.jappgeo.2014.01.016>
- Yıldırım, E., Saatçılar, R., & Ergintav, S. (2017). Estimation of seismic quality factor: Artificial neural networks and current approaches. *Journal of Applied Geophysics*, 136, 269–278. <https://doi.org/10.1016/j.jappgeo.2016.11.010>
- Zhang, C., & Ulrych, T. J. (2002). Estimation of quality factors from CMP records. *Geophysics*, 67(5), 1542–1547. <https://doi.org/10.1190/1.1512799>
- Zoback, M. D., & Zinke, J. C. (2002). Production-induced normal faulting in the Valhall and Ekofisk oil fields. *Pure and Applied Geophysics*, 159(1), 403–420. <https://doi.org/10.1007/PL00001258>